Acoustomicrofluidic Synthesis of Pristine Ultrathin Ti3C2Tz MXene Nanosheets and Quantum Dots

Hossein Alijani, Amgad R. Rezk, Mohammad Mehdi Khosravi Farsani, Heba Ahmed, Joseph Halim, Philipp Reineck, Billy J. Murdoch, Ahmed El Ghazaly, Johanna Rosén and Leslie Y. Yeo

Tweet

LINKÖPING UNIVERSITY

Chemical-Free Acoustomicrofluidic Synthesis of Ultrathin Pristine Ti$_3$C$_2$T$_z$ MXene Nanosheets and Quantum Dots

Hossein Alijani,[†] Amgad R. Rezk,[†] Mohammad Mehdi Khosravi Farsani,[†] Heba Ahmed,[†] Joseph Halim,[‡] Phillip Reineck,[¶] Billy J. Murdoch,[§] Ahmed El-Ghazaly,[‡] Johanna Rosen,[*,‡] and Leslie Y. Yeo [*,†]

[†]*Micro/Nanophysics Research Laboratory, RMIT University, Melbourne, VIC 3000, Australia*

[‡]*Thin Film Physics Division, Department of Physics, Chemistry, and Biology (IFM), Linköping University, Linköping SE-58183, Sweden.*

[¶]*ARC Centre of Excellence for Nanoscale BioPhotonics, School of Science, RMIT University, Melbourne, VIC 3001, Australia.*

[§]*RMIT Microscopy & Microanalysis Facility, STEM College, RMIT University, Melbourne, VIC 3000, Australia*

E-mail: johanna.rosen@liu.se; leslie.yeo@rmit.edu.au

Abstract

The conversion of layered transition metal carbides and/or nitrides (MXenes) into zero-dimensional structures with thicknesses and lateral dimensions of a few nanometers allows these recently discovered materials with exceptional electronic properties to exploit the additional benefits of quantum confinement, edge effects, and large surface area. Conventional methods for the conversion of MXene nanosheets and quantum dots,

however, involve extreme conditions such as high temperatures and/or harsh chemicals that, among other disadvantages, lead to significant degradation of the material as a consequence of their oxidation. Herein, we show that the large surface acceleration—on the order of 10 million g's—produced by high-frequency (10 MHz) nanometer-order electromechanical vibrations on a chipscale piezoelectric substrate is capable of efficiently nebulising, and consequently, dimensionally reducing a suspension of multilayer $Ti_3C_2T_z$ (MXene) into predominantly monolayer nanosheets and quantum dots whilst, importantly, preserving the material from any appreciable oxidation. As an example application, we show that the high purity of the MXene quantum dots produced using this novel room-temperature chemical-free synthesis method exhibit superior performance as electrode materials for electrochemical sensing of hydrogen peroxide compared to the highly-oxidised samples obtained through conventional hydrothermal synthesis. The ability to detect concentrations as low as 5 nM is a ten-fold improvement to the best reported performance of $Ti_3C_2T_z$ MXene electrochemical sensors to date.

Keywords

$Ti_3C_2T_z$ MXene, quantum dots, nanosheets, surface reflected bulk waves, H_2O_2 sensing

Introduction

MXenes are a new family of 2D inorganic materials comprising early transition metal carbides and nitrides with the chemical formula $M_{n+1}X_nT_z$ (M: early transition metal; X: C and/or N; n = 1, 2, 3; T_z: surface termination groups such as O, OH, F and/or Cl)[1–7] typically obtained by selectively etching the A-layer (A being a group 13 or 14 element) from the parent MAX phase.[1,8,9] MXenes have received considerable attention of late owing to their outstanding electronic properties, high conductivity and excellent electrochemical activity.[10]

Together with the hydrophillicity of their surface termination groups, MXenes are endowed with very high capacitance, therefore rendering them highly promising high-performance electrode materials for energy storage applications (e.g., lithium- or sodium-ion batteries and supercapacitors).[11–16] In addition, the material has also been explored for electromagnetic shielding,[17] catalysis,[18,19] energy conversion,[20] CO_2 capture[21] and ionic separation,[22] among other applications.[23]

In the same way that dimensional reduction of 2D materials to nanosheets and quantum dots (QDs) has led to a diversification of their use by capitalising on their large surface area and unique quantum confinement and edge effects[24–26] while retaining the advantages of the parent material, MXene nanosheets, and, in particular, MXene quantum dots (MQDs), which display photoluminescence and electrochemiluminescence characteristics[27–30] in addition to being biocompatible, have been explored for ion sensing,[31–33] photothermal therapy,[34] bioimaging,[31,35,36] biosensing[37] and enzymatic detection.[38,39] In addition, MQDs have also been incorporated into composite structures to enhance their photocatalytic and electro-catalytic properties,[40–44] or to enhance charge injection, for example, in perovskite solar cells.[45]

The most common method by which MQDs and nanosheets are synthesized is through the delamination of multilayered MXene through solvothermal[28,29,33,39] or hydrother-mal[27,30,31,35,37,38,40–52] processes, microwave-assisted irradiation[53] or electrochemical etch-ing.[54] These methods are, however, not only lengthy, requiring agitation or sonication for many hours to days, but typically also involve temperatures at or beyond 100 °C and hazardous chemicals including acids, bases or organic solvents, thereby necessitating post-synthesis wash and separation steps for their removal. More importantly, it is worth noting that a major drawback of such methods is the severe oxidation of $Ti_3C_2T_z$ during syn-thesis wherein the TiO_2 content in the synthesized MQD samples can often be as high as 40–80%.[27–29,32,35,37,38,40,43,46–50]

Herein, we report a novel chemical-free acoustomicrofluidic method for room-temperature

delamination of single- to few-layer $Ti_3C_2T_z$ MXene nanosheets and their conversion to MQDs that preserves the integrity of the material in terms of minimising its oxidation during the synthesis process. The method, illustrated schematically in Fig. 1, relies on the use of a recently-discovered class of nanometer-amplitude high frequency (MHz-order) hybrid sound waves known as surface reflected bulk waves (SRBWs),[55] whose extraordinary 10^8 m/s^2 surface acceleration and strong 10^7 V/m evanescent electric field[56] has been shown to be an incredibly versatile mechanism for manipulating fluids as well as bulk and 2D crystals,[57] including the exfoliation of bulk transitional metal dichalcogenides,[58–61] and more recently, $Ti_3C_2T_z$ from $Ti_3AlC_2T_z$.[62] In contrast to this preceding work wherein the surface acoustic waves played a role in facilitating the protonation of lithium fluoride into hydrofluoric acid, which, in turn, selectively etched Al from Ti_3AlC_2, therefore converting it into $Ti_3C_2T_z$, we show in this work direct mechanical delamination and lateral cleaving of multilayer MXenes into monolayer and few-layer nanosheets and MQDs without the need for chemical (polar aprotic solvents such as dimethyl sulfoxide (DMSO)[63] or organic bases such as tetrabutylammonium hydroxide (TBAOH)[64]) or *in situ* (Li ions present in the etchant[65]) intercalants.

Besides revealing their low (approximately 14%) $TiO_{2-x}F_x$ content, which is comparable to that found in the pristine MXene feedstock (around 14%), we show that the MQDs we synthesize have superior performance as electrode materials in electrochemical sensors compared to the MQDs produced using the hydrothermal method which contained a high proportion of $TiO_{2-x}F_x$; we note that MXenes have been employed to date for improving direct electron transfer and for enzyme immobilisation to increase their bioactivity in electrochemical sensors given their superior electronic properties, large surface area and biocompatibility.[66] Here, we demonstrate their use for the detection of hydrogen peroxide (H_2O_2) given its importance as a common reactive oxygen species in biological systems and as a byproduct of several oxidase reactions, such as glucose oxidation.[66] Moreover, the strong oxidising properties of H_2O_2 are likely to result in further oxidation of MXene during sensing, which, in

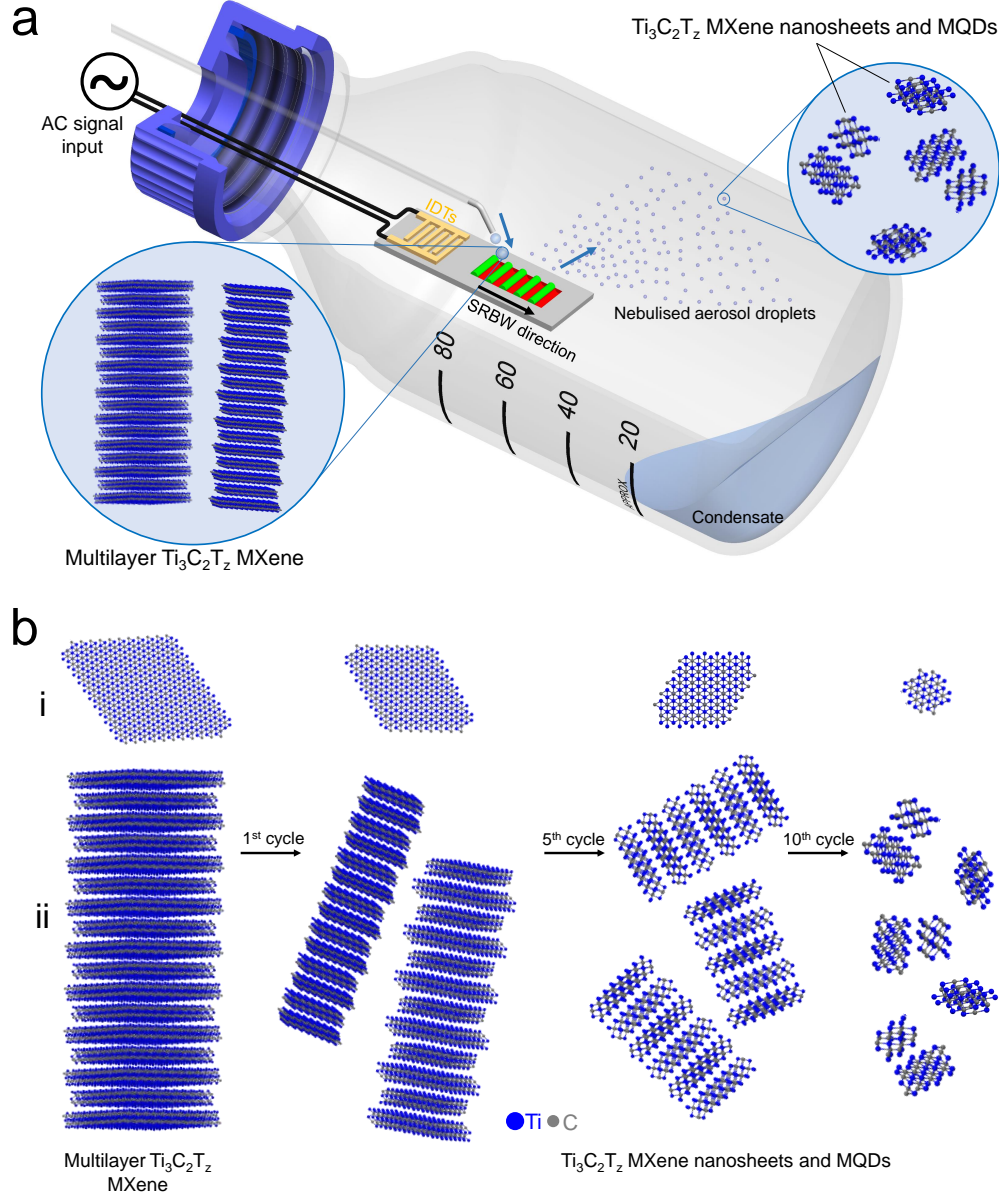Figure 1: (a) Schematic illustration of the experimental setup in which a multilayer $Ti_3C_2T_z$ MXene sample is continuously delivered to the SRBW device, atop which it nebulises to form aerosol droplets of delaminated and cleaved $Ti_3C_2T_z$ which condense within the glass bottle enclosure. (b) Successive renebulisation of the condensate collected over many cycles is observed to (i) laterally cleave, and, (ii) delaminate the sample into progressively smaller and thinner MXene nanosheets and MQDs.

turn, leads to additional degradation in its performance, and thus the importance of using as pristine as possible MQDs with minimal oxidation to begin with. Additionally, we note that the need for pristine MQDs with low TiO_2 content has also been underscored in other work

utilising MQDs for cancer therapy as catalytic materials for OH$^\bullet$ free radical generation in the presence of H_2O_2 produced in tumour microenvironments since it has been found that oxidised MQDs exhibit significant loss in their catalytic activity.[67]

Results and Discussion

The initial multilayer MXene feedstock, which possess flakes with typical thicknesses and lateral dimensions on the order of a few microns (see, for example, the representative scanning electron microscopy (SEM) and transmission electron microscopy (TEM) images in Supplementary Fig. S1), can be seen to be progressively cleaved laterally and delaminated with successive nebulisation cycles, as seen in Fig. 2. More specifically, after 1, 5 and 10 nebulisation cycles, we observe the number of layers of the resultant nanosheets to be thinned to 8.5 ± 2.6 nm, 4.8 ± 1.0 nm and 1.1 ± 0.4 nm, and their mean diameter cleaved to 68.4 ± 16.9 nm to 27.1 ± 11.9 nm and 10.7 ± 5.6 nm, respectively. Besides facilitating the ability to tune the nanosheet dimension of the MXene nanosheets that are produced, the acoustomicrofluidic synthesis technique constitutes an efficient method for the generation of predominantly single-layer, and, at most, two-layer MQDs (the thickness of a Ti_3C_2 MXene monolayer being approximately 0.98 nm[68]), with mean diameters of 10.7 ± 5.6 nm obtained at the end of 10 nebulisation cycles. TEM images of the MQDs obtained, along with the selected area electron diffraction (SAED) pattern showing the hexagonal structure typical of MXenes, can be found in Supplementary Fig. S2.

The x-ray diffraction (XRD) spectra in Fig. 3(a) shows the typical MXene (002) peak at 9° in the pristine multilayer feedstock that, together with the (004) peak, indicates its layered structure in agreement with the SEM and TEM images in Supplementary Fig. S1, and which, together with the rest of the peaks associated with the (006), (008) and (110) planes, conform to that reported in the literature for $Ti_3C_2T_z$ MXene.[1,69,70] Upon its nebulisation to produce the delaminated MXene nanosheets and MQDs, the (002) peak can be seen to shift
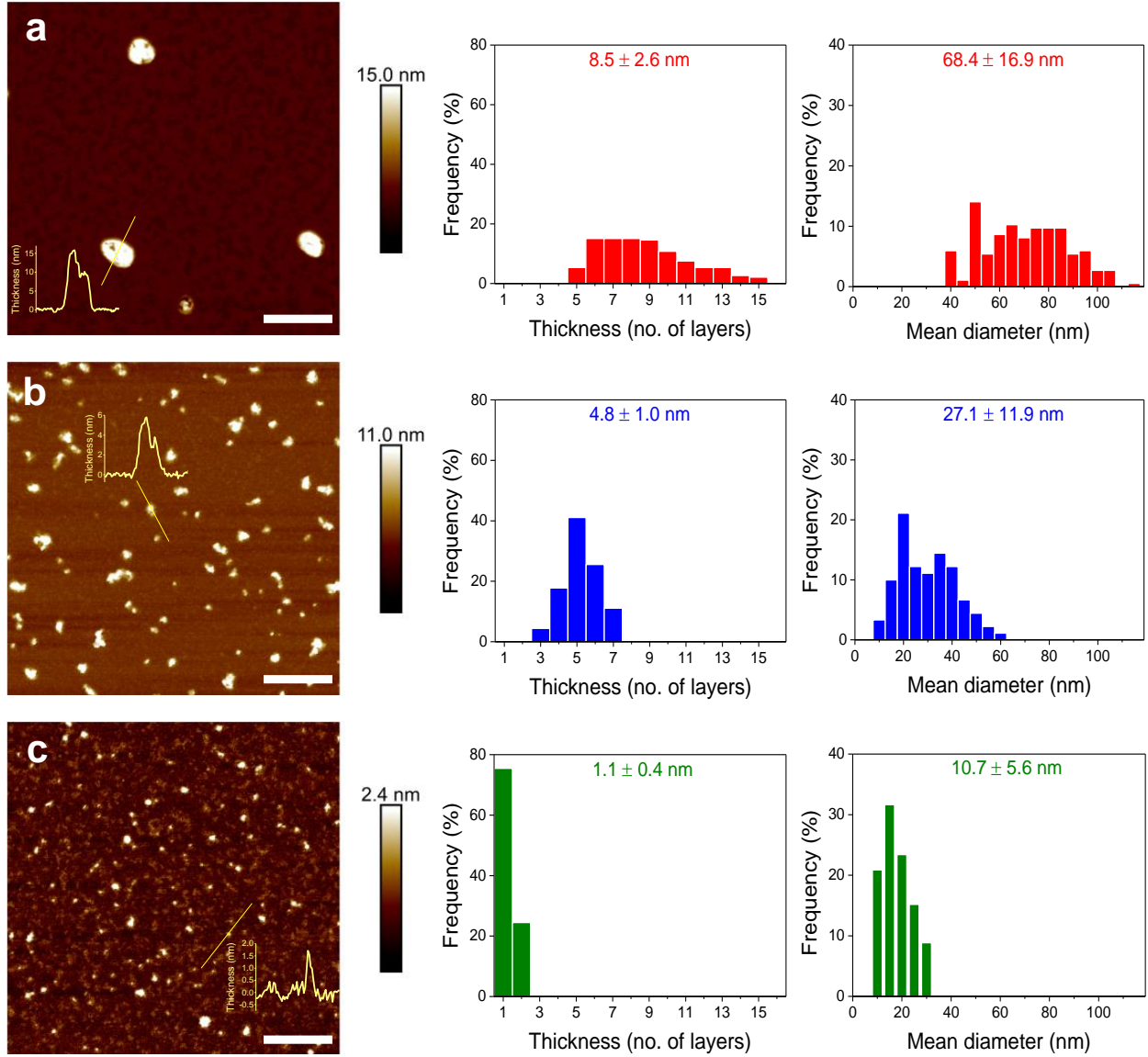
Figure 2: Representative atomic force microscopy (AFM) images (including sample thickness profiles) and corresponding thickness (centre; in terms of numbers of atomic layers) and mean lateral diameter (right) measurement distributions of the acoustically-synthesized MXene nanosheets and MQDs after (a) 1, (b) 5, and (c) 10 nebulisation cycles. The mean values of the distributions are indicated at the top of the histograms and scale bars denote lengths of 200 nm.

to a lower angle of approximately 7° following the first nebulisation cycle and to 6.1° after 10 nebulisation cycles. This peak, as well as the (004) peak, can also be seen to broaden slightly and to decrease in intensity, which could likely be due to increasing intercalation of the solvent between the delaminated layers,[63] although we note that these observations

7
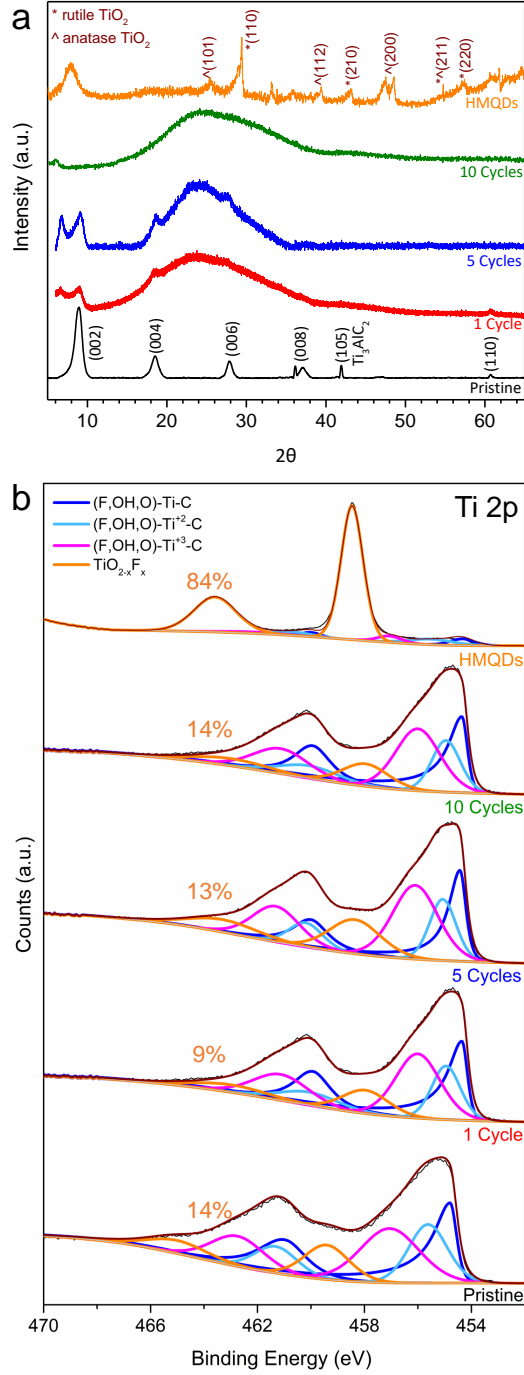
Figure 3: (a) XRD and (b) high resolution XPS (Ti 2p region) of the pristine multilayer MXene feedstock, the MXene nanosheets after 1 and 5 nebulisation cycles, the MQDs after 10 nebulisation cycles, and the HMQDs. Also indicated in the XPS spectra are the areal percentages of the $TiO_{2-x}F_x$ species for each case.

have also been attributed in the literature to the delamination of MXene to MQDs and the increasing presence of monolayer structures.[28,35,37] Further, we observe the appearance of an

additional peak at 9° for the nanosheets produced after 1 and 5 nebulisation cycles, which can likely be due to their stacking on top of each other as a result of drop casting multiple samples during sample preparation;[71] we note the repeated drop casting onto the glass slide also produced a thicker film that gave rise to a large background signal associated with the broad peak between approximately 16° to 38° for the nebulised samples that was not present in the pristine sample. In addition, we also observe the disappearance of the (110) peak beyond 5 nebulisation cycles; while this has been claimed to indicate complete delamination and the absence of any crystallographic stacking between the MQDs,[35] it is more likely that the suppression of the peak arises as a consequence of sample texture and orientation.[72]

Deconvolution of the peaks in the high resolution x-ray photoelectron spectroscopy (XPS) spectra associated with the Ti 2p region of all the samples in Fig. 3(b) reveals the change in the areal percentage of the MXene assigned species, i.e., (F, OH, and/or O)$-$Ti$-$C, (F, OH, and/or O)$-$Ti$^{2+}-$C, (F, OH, and/or O)$-$Ti$^{3+}-$C, and TiO$_{2\text{-x}}$F$_{\text{x}}$,[73,74] with successive nebulisation cycles compared with that in the pristine multilayer feedstock and hydrothermally-synthesized (HMQD) samples. In particular, we note the similarity in the composition between the acoustically-synthesized MXenes with that of the pristine sample, indicating minimal degradation of the material due to oxidation, as can be seen from the TiO$_{2\text{-x}}$F$_{\text{x}}$ content of the acoustically-synthesized MXenes (9%, 13%, and 14% for 1, 5 and 10 nebulisation cycles, respectively), which, after accounting for measurement tolerances, is not appreciably different from that of the pristine feedstock (14%). This is in stark contrast to those produced via conventional hydrothermal synthesis, which exhibited extremely high levels of oxidation (84%) consistent with that reported in the literature (typical values between 40% and 80% have been reported in the literature for the equivalent oxide and oxyfluoride (TiO$_2$ and/or TiO$_{2\text{-x}}$F$_{\text{x}}$) species[27–29,32,35,37,38,40,43,46–50]). As further confirmation, we note that the significant difference in the oxidation levels between the acoustically-synthesized MXenes and HQMDs is also evident in the aforementioned XRD spectra in Fig. 3(a), wherein it can be seen that, in addition to the shift in the (002) down to 7.8° as a result of solvent

intercalation, multiple peaks associated with the rutile and anatase phases of TiO_2[75] are present for the HQMD samples that are notably absent in their acoustically-synthesized counterparts.

Figure 4 reports the UV-vis absorption, and, fluorescence (FL) and photoluminescence (PL) emission spectra of the MQDs after the tenth nebulisation cycle. As expected, we observe strong absorption in the UV region, with maximum absorbance around 213 nm, and excitation-dependent fluorescence emission with a maximum occurring at an excitation of 360 nm. It can also be seen from the inset of Fig. 4(a) that the MQDs, while transparent under ambient excitation, are strongly fluorescent under UV excitation at 365 nm. These measurements also allow us to estimate a quantum yield for the MQDs of 2.5% (see the Supplementary Information for details of this calculation). Furthermore, we note the considerable difference in the PL intensity in Fig. 4(b) that oxidation in the sample produces, with substantially lower PL intensities observed for the high $TiO_{2-x}F_x$ content of the HMQDs compared to that obtained with the high-purity acoustically-synthesized MQDs. Although more broadly dependent on the species and surface states, the longer emission lifetimes, as seen from the decay in the PL signal of the HQMDs in the inset of Fig. 4(b) (3.9 ns compared to 3.4 ns for the acoustically-synthesized MQDs, which are comparable to values reported in the literature[27,28,30,31,37,44,48]), can also be attributed to its higher oxide content.[28]

Given the considerably lower $TiO_{2-x}F_x$ content of the acoustically-synthesised MQDs, we anticipate their electrochemical sensing performance to be superior to that of the HMQDs. To verify this assertion, we compare the performance of both the MQDs we synthesize and the HMQDs as electrode materials for improving direct electron transfer and maintaining enzyme bioactivity[66] for the detection of H_2O_2 as a model analyte. The improvement in electrochemical sensing with the incorporation of MXene can immediately be seen in the increasing square wave voltammetry peak currents with increasing H_2O_2 concentrations with both electrode configurations in Fig. 5(a,b). We observe, however, the stark contrast in the current range of the Naf/MQD/GCE electrode configuration compared to that obtained with
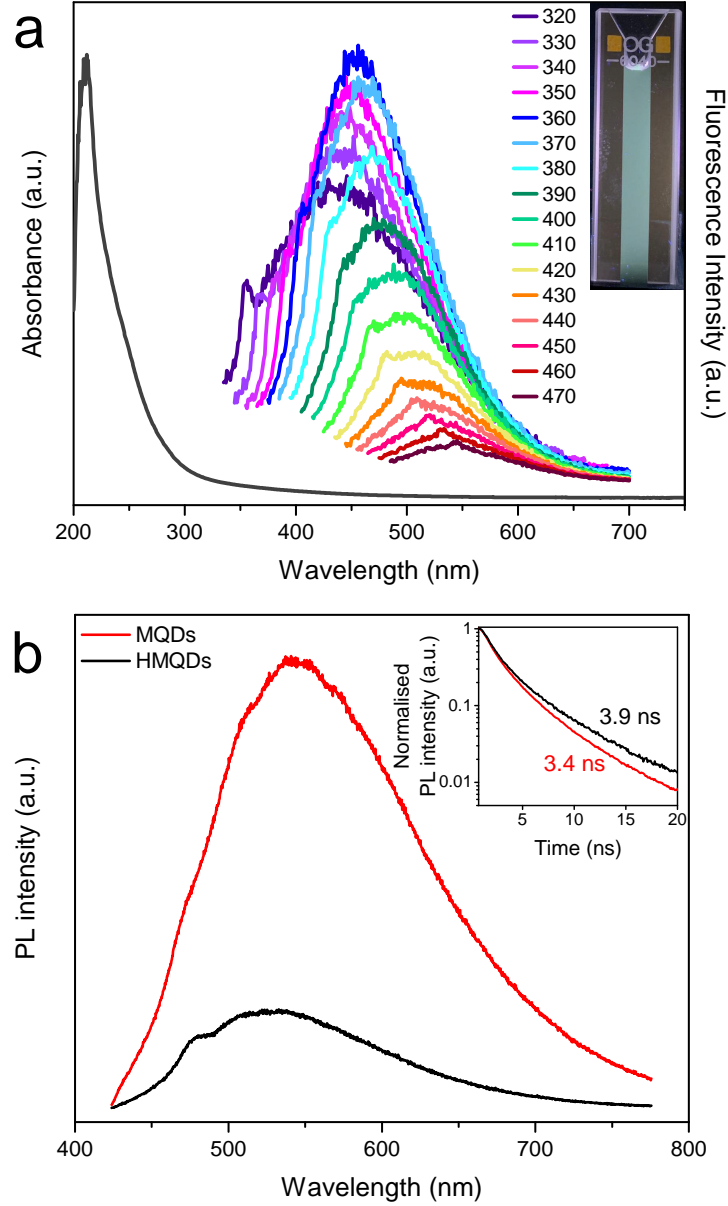
Figure 4: (a) UV–vis absorption (black curve, left axis), fluorescence emission (coloured curves, right axis; the legend specifying the corresponding excitation wavelengths in nm), and, (b) photoluminescence (PL) spectra of the acoustically-synthesized MQDs acquired after 10 nebulisation cycles (1.1 ± 0.4 nm thickness; 10.7 ± 5.6 nm in diameter). In (a), excitation-dependent fl017oescence emission is evident with the maximum occurring at 360 nm excitation; the inset shows an image of the MQD suspension excited with a 365 nm UV lamp. In (b), the excitation wavelength is 400 nm; also shown is the corresponding spectra for HMQDs, which due to its high $TiO_{2-x}F_x$ composition, results in considerably weaker PL emission intensity; the corresponding lifetimes of the MQDs and HQMDs, from the PL decay curves shown in the inset, are 3.4 and 3.9 ns, respectively.

x

11

the Naf/HMQD/GCE electrode configuration, whose poor current response is likely due to its significantly higher $TiO_{2-x}F_x$ content. The superior performance of the Naf/MQD/GCE electrode can also be seen in the linear regression slope of the current response plots in Fig. 5(c), which is approximately 5- to 6-fold greater than that for the Naf/HMQD/GCE electrode over the range 5–24 nm and 24 nm–54.4 μM. We also note that the ability to detect H_2O_2 down to a concentration of 5 nM with the Naf/MQD/GCE configuration is one order of magnitude smaller than the smallest value reported in the literature for $Ti_3C_2T_z$ MXene;[76] a detailed comparison in the detection performance with other $Ti_3C_2T_z$ MXene electrodes can be found in Table S2 in the Supplementary Information. Moreover, cyclic voltammograms of the electrodes in Supplementary Fig. S3 reveal a stable redox peak at approximately 0.2 V for the Naf/MQD/GCE and Naf/HMQD/GCE electrodes in comparison to the bare Nafion-coated electrode (Naf/GCE) in which the redox peak is absent, therefore demonstrating their electroactivity towards H_2O_2 and hence their ability for its detection.

Conclusions

MXene nanosheets and quantum dots offer the possibility of combining the advantages of enhanced electronic properties, high conductivity and superior electrochemical activity, with the benefits of quantum confinement, edge effects and large surface area. Conventional methods for synthesizing these materials, which include the ubiquitous solvothermal and hydrothermal methods, besides being lengthy and requiring elevated temperatures and hazardous chemicals, however, result in significant oxidation of the sample to TiO_2, therefore considerably compromising the purity of the material, leading to a degradation of its performance in various applications. In this work, we have reported a new chemical-free, room-temperature method for delaminating multilayer MXene into predominantly monolayer MQDs by uniquely exploiting the large mechanical forcing that accompanies the nebulisation of the sample driven by high frequency acoustic waves. In addition to relatively faster
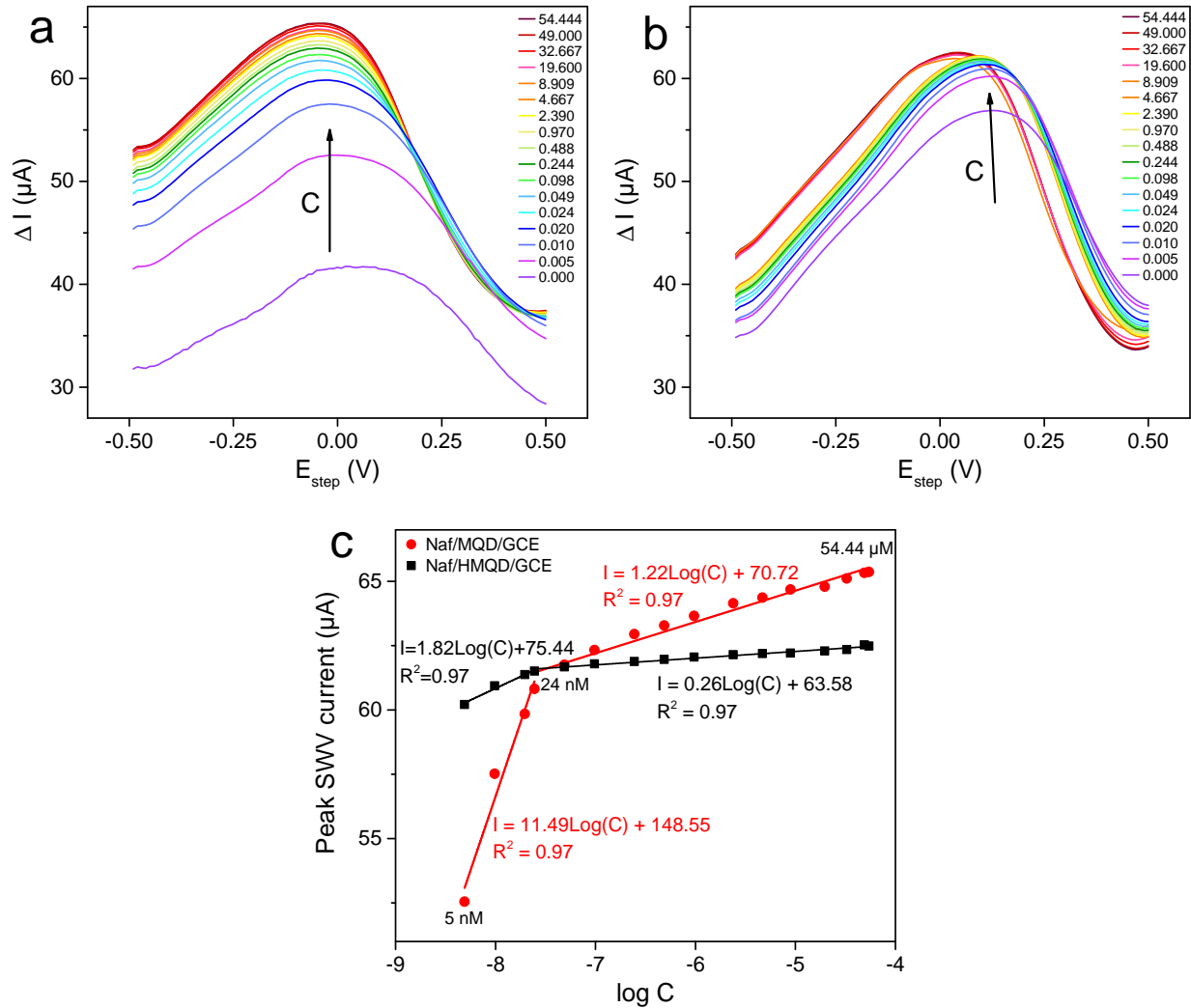
12

Figure 5: (a,b) Square wave voltammetry curves for the (a) Naf/MQD/GCE, and, (b) Naf/HMQD/GCE configurations in 0.1 M PBS with varying H_2O_2 concentrations (specified in μM); the arrows show the trend observed for increasing H_2O_2 concentrations. (c) Current response and hence detection responsiveness for both the Naf/MQD/GCE (red lines) and Naf/HMQD/GCE (black lines) configurations.

synthesis times, the method is easily scalable with massive device parallelisation given the miniaturised footprint of the chipscale device and its low costs (around US$1/device by exploiting the economies-of-scale associated with the mass nanofabrication). More importantly, we show that the MQDs synthesized through this technique does not lead to appreciable oxidation of the material. In addition to exhibiting strong UV absorption and excitation-dependent fluroescence, we show that the high purity of the material leads to their markedly

better performance as electrode materials for electrochemical sensing, in particular, that of H_2O_2, wherein we show the possibility of detecting concentrations down to 5 nM, which is the lowest value achieved with $Ti_3C_2T_z$ MXene electrochemical sensors to date.

Materials and Methods

Materials

Ti$_3$AlC$_2$ MAX phase was synthesized by a solid state reaction between Ti (-325 mesh, 99.999 wt.% purity; Alfa Aesar, Kandel, Germany), TiC (-325 mesh, 99.5 wt.% purity; Alfa Aesar, Kandel, Germany) and Al (-325 mesh, 99.5 wt.% purity; Alfa Aesar, Kandel, Germany) at a molar ratio of 1:2:1, respectively, corresponding to a stoichiometry of Ti$_3$AlC$_2$. The powders were first mixed manually in an agate mortar, following which they were placed in an alumina crucible and inserted in a horizontal tube furnace. The furnace was heated, under a 5 sccm Ar flow, at 5 °C/min to 1450 °C, at which temperature it was held for 120 min. After furnace cooling, the sample was crushed using a mortar and pestle, and sieved through a 450-mesh sieve.

To synthesize the multilayer Ti$_3$C$_2$ feedstock, 1 g of Ti$_3$AlC$_2$ powder (-450 mesh) was immersed slowly in a polytetrafluoroethylene (PTFE) bottle containing 10 ml of 50 wt./vol.% hydrofluoric acid (HF; Sigma Aldrich Corp., St. Louis, USA). The mixture was then stirred using a PTFE-coated magnetic stirrer bar for 24 h at room temperature and the resulting mixture washed with N$_2$ deaerated deionised (DI) water for several cycles till the pH was approximately 6 (typically, 8 cycles were needed). In each washing cycle, 40 ml of DI water was added to the multilayer powder in a centrifuge tube, hand-shaken for 1 min, and centrifuged at 5000 rpm for 1 min, from which the supernatant was decanted. Following washing, the colloidal solution was vacuum-filtered onto a nanoporous polypropylene membrane (3501 Coated PP, 0.064 µm pore size; Celgard LLC, Charlotte, NC, USA), from which the powder was collected and left to dry in vacuum oven at 100 °C for 24 h.

Device Fabrication and Operation

A schematic depiction of the experimental setup comprising the SRBW device enclosed in a Parafilm-sealed (Bemis Company Inc., Neenah, WI, USA) 100 ml glass bottle is shown in

Fig. 1(a). The device consists of a 30 mm $\times$ 11 mm $\times$ 0.5 mm single-crystal piezoelectric lithium niobate substrate (128° Y-rotated, X-propagating LiNbO$_3$; Roditi Ltd, London, UK) on which an interdigitated transducer (IDT) electrode with 96 μm aperture is fabricated by sputter depositing (SPI-Module Sputter Coater; Structure Probe Inc., West Chester, PA, USA) a 10-nm-thick chromium adhesion layer followed by a 200-nm-thick gold layer and subsequently wet etching an IDT pattern comprising 60 straight interleaved finger pairs using standard photolithography; the width of each IDT finger and the spacing between two adjacent fingers are equal to a quarter of the SRBW wavelength $\lambda \approx 400$ μm, which is then related to the resonant frequency $f \approx 10$ MHz by the phase speed of the sound wave in LiNbO$_3$.

Before commencing the experiment, the device was first thoroughly washed in acetone and isopropyl alcohol (Sigma-Aldrich Pty. Ltd., Castle-Hill, New South Wales, Australia), then dried and carefully placed in the 100 ml glass bottle, with its electrical connections passed through a hole in its lid (Fig. 1(a)). A 20 ml suspension of multilayer Ti$_3$C$_2$T$_z$ MXene feed-stock at a concentration of 1 mg/ml in ethanol (Sigma-Aldrich Pty. Ltd., Castle-Hill, NSW, Australia) was continuously introduced onto the chip with a glass syringe through PTFE tubing (2 mm OD, Cole-Parmer, IL, USA) and a hypodermic syringe needle (24G $\times$ 1", Terumo Corp., Laguna, Philippines) at a delivery rate of approximately 1 ml/min. Prior to loading the syringe, the MXene suspension was bath-sonicated for 20 mins to achieve a stable dispersion; the syringe was also periodically agitated during the experiment to avoid sedimentation of the MXene. Ethanol was used as the organic solvent as it is known to facilitate high dispersibility of the MXene in addition to preventing its degradation.[77] The low surface tension of ethanol also allows the suspension to spread evenly into a thin film on the surface of the SRBW device, thus allowing more uniform exposure of the material to the acoustic waves, which, in turn, leads to better monodispersivity in the aerosol size distribution as the suspension is nebulised by the SRBW.[78]

The nebulisation process,[55,78] which typically results in the generation of a mist of aerosol

16

droplets with a typical mean diameter of 1–5 μm, is initiated by applying a 30 V_{rms} oscillating electrical signal at the 10 MHz resonance frequency from a signal generator (SML01; Rhode & Schwarz, North Ryde, NSW, Australia) coupled to an amplifier (LYZ-22+; Mini Circuits, Brooklyn, NY, USA). Given their exposure to the tremendous 10^8 m/s^2 acceleration on the surface of the device as the SRBW transverses it, the multilayer MXene flakes in the thin suspension film on the substrate prior to being nebulised are subjected to large compressional and shear stresses that simultaneously cleaves the flakes laterally and delaminates them into smaller and thinner entities (Fig. 1(b)), which are then caught up in the aerosol droplets that are generated as the film itself nebulises. Given the enclosed setup, the MXene-laden aerosol droplets typically condense along the walls of the glass bottle and accumulate in a pool at its bottom before subsequently being collected and renebulised. Each nebulisation and condensation cycle consists of complete nebulisation of the entire 20 ml suspension, which, at a rate of approximately 1 ml/min, takes around 20 mins. Up to 10 cycles were performed, with the resultant MXene nanosheets becoming progressively smaller and thinner with every cycle to the point where predominantly monolayer MQDs were obtained at the end of the 10th cycle (Fig. 1(b)).

Characterisation

To show such dimensional reduction with successive nebulisation cycles, the condensate was sampled after the 1st, 5th and 10th cycles and centrifuged (5430; Eppendorf, Hamburg, Germany) at 3500 rpm for 20 mins, from which the supernatant containing the MXenes was extracted and approximately 1 ml (considerably less for atomic force microscopy (AFM)) was drop-casted onto a mica sheet for analysis under AFM (Dimension Icon; Bruker Corp., Billerica, MA, USA), a glass slide for XRD (D8 Advance; Bruker Corp., Billerica, MA, USA), and a silicon substrate for XPS (Kratos AXIS Supra; Kratos Analytical Ltd., Manchester, UK). For the AFM measurements, a minimum of 100 particles were analysed to provide representative lateral and thickness dimensions. XPS was collected using a monochromated

Al Kα X-ray source (1486.7eV) with a step size of 0.050 eV. The binding energy (BE) scale of the Ti 2p XPS spectra, on the other hand, was referenced to the Fermi-edge (E_F), which was set to a BE of 0 eV; peak fitting was carried out using CasaXPS (Version 2.3.16 RP 1.6; Casa Software Ltd., Teignmouth, UK) in the same manner as that in previous work.[73,74]

Pristine multilayer MXenes were imaged using SEM (Phillips/FEI XL30 SEM-FEG; Thermo Fisher Scientific, Hillsboro, OR, USA) operating at an accelerating voltage of 5 kV and TEM (JEM-1010; JEOL, Frenchs Forest, NSW, Australia) operating at 100 kV. High resolution TEM imaging of these and the MQDs, on the other hand, were conducted using a scanning transmission electron microscope (JEM-2100F; JEOL, Frenchs Forest, NSW, Australia) operating at 200 kV.

Fluorescence emission and absorption spectra of the MQDs were obtained using a spectrofluorometer (FluoroMax-4, Horiba Jobin Yvon SAS, Edison, NJ, USA) and a UV-Vis spectrophotometer (Cary 60, Agilent Technologies Inc., Santa Clara, CA, USA), respectively. For time-resolved fluorescence decay measurements, the MQD suspensions were illuminated in dedicated cuvettes (Semi-Micro Type 9FL, FireflySci Inc., Staten Island, NY, USA) with a weakly focused 2 mW laser beam (WhileLase SC400-8, NKT Photonics Ltd., Birkerød, Denmark) at a wavelength of 400 nm; the fluorescence signal was fibre-coupled, filtered with a 550 nm optical long-pass filter (Edmund Optics, Barrington, NJ, USA) and detected with either a spectrometer (Spectra Pro; Princeton Instruments, Trenton, NJ, USA) fitted with a CCD camera (Pixis:100; Princeton Instruments, Trenton, NJ, USA) or an avalanche photodiode (SPCM-AQRH-14; Excelitas Technologies Corp., Waltham, MA, USA), and analysed with a correlator card (TimeHarp 260; PicoQuant, Berlin, Germany) for time-resolved measurements.

Electrochemical Sensing

All electrochemical sensing experiments were carried out on a laboratory potentiostat (VSP; BioLogic, Seyssinet-Pariset, France) with a three-electrode configuration compris-

ing a Ag/AgCl in 3 M potassium chloride (KCl) reference electrode, a counter platinum (Pt) wire electrode (0.5 mm diameter; CH instruments Inc., Austin, TX, USA), and a 3-mm-diameter modified glassy carbon electrode (GCE) as the working electrode. Prior to the measurements, the GCEs were polished in a 1.0, 0.5 and 0.03 μm alumina slurry in sequence, bath-sonicated in ethanol for 20 mins, rinsed with water (18.2 MΩ·cm at 25 °C; Milli-Q®, Merck KGaA, Darmstadt, Germany), and blow-dried. To prepare the modified GCE, 30 μl of the MQD suspension after the 10th cycle was drop casted onto the GCE in 1 μl increments and left to dry before the next increment. This was followed by drop casting 2 μl of Nafion™ 117 solution (approximately 5% in a mixture of lower aliphatic alcohols and water; Sigma-Aldrich Pty. Ltd., St Louis, MO, USA), and allowing it to dry at room temperature under cover to protect it from dust. Cyclic voltammetry (CV) and square wave voltammetry (SWV) from -0.5 to 0.5 V were conducted for the detection of H_2O_2 by adding small volumes of this target analyte (30 wt./wt.% H_2O_2; Chem-Supply Pty. Ltd., Gillman, SA, Australia) to 20 ml 0.1 M phosphate buffered saline (BupH™, 0.1M sodium phosphate, 0.15M sodium chloride, pH 7.2; Thermo Fisher Scientific, Rockford, IL, USA) solution followed by stirring with a magnetic bar at 500 rpm for 2 mins to produce a homogeneous H_2O_2 solution with concentrations across the range 5 nM to 54 μM. Measurements were recorded with EC-Lab software (v11.25, BioLogic, Seyssinet-Pariset, France).

To compare the extent of oxidation and its consequence on the sensing performance of the acoustically-synthesized MQDs with those obtained via a commonly-used synthesis method, we also repeated the aforementioned experiments with MQDs produced via a conventional hydrothermal process reported in the literature.[35,38,41,42,44,47] Briefly, 25 mg of the same bulk multilayer $Ti_3C_2T_z$ MXene feedstock was dispersed in 25 ml distilled water (UltraPure™; Invitrogen, Grand Island, NY, USA) and bath sonicated for 30 mins to make a 1 mg/ml suspension, to which ammonium hydroxide was gradually added to adjust the solution pH to 9.0. The solution was then transferred to a PTFE-lined stainless steel autoclave and placed in an oven at 100 °C for 6 h, following which it was left to cool down to room temperature.

19

The HMQDs synthesized using this method were then collected by filtering the solution through a 0.22 μm microporous Nylon membrane (GVS Life Sciences, Sanford, ME, USA). The modified GCE electrode with these HMQDs was prepared in the same way as that for the acoustically-synthesized MQDs.

Acknowledgement

Supporting Information Available

Supporting Information Available: Electon microscopy images of the pristine $Ti_3C_2T_z$ feedstock and MQDs; quantum yield calculation; XPS peak deconvolution analysis in the Ti 2p region; H_2O_2 sensing. This material is available free of charge via the Internet at http://pubs.acs.org.

References

1. Naguib, M.; Kurtoglu, M.; Presser, V.; Lu, J.; Niu, J.; Heon, M.; Hultman, L.; Gogotsi, Y.; Barsoum, M. W. Two-dimensional Nanocrystals Produced by Exfoliation of Ti_3AlC_2. *Adv. Mater.* **2011**, *23*, 4248–4253.

2. Naguib, M.; Mochalin, V. N.; Barsoum, M. W.; Gogotsi, Y. 25th Anniversary Article: MXenes: a New Family of Two-dimensional Materials. *Adv. Mater.* **2014**, *26*, 992–1005.

3. Anasori, B.; Xie, Y.; Beidaghi, M.; Lu, J.; Hosler, B. C.; Hultman, L.; Kent, P. R.; Gogotsi, Y.; Barsoum, M. W. Two-dimensional, Ordered, Double Transition Metals Carbides (MXenes). *ACS Nano* **2015**, *9*, 9507–9516.

4. Hope, M. A.; Forse, A. C.; Griffith, K. J.; Lukatskaya, M. R.; Ghidiu, M.; Gogotsi, Y.; Grey, C. P. NMR Reveals the Surface Functionalisation of Ti_3C_2 MXene. *Phys. Chem. Chem. Phys.* **2016**, *18*, 5099–5102.

5. Halim, J.; Cook, K. M.; Eklund, P.; Rosen, J.; Barsoum, M. W. XPS of Cold Pressed Multilayered and Freestanding Delaminated 2D Thin Films of $Mo_2TiC_2T_z$ and $Mo_2Ti_2C_3T_z$ (MXenes). *Appl. Surf. Sci.* **2019**, *494*, 1138–1147.

6. Lu, J.; Persson, I.; Lind, H.; Palisaitis, J.; Li, M.; Li, Y.; Chen, K.; Zhou, J.; Du, S.; Chai, Z., *et al.* $Ti_{n+1}C_n$ MXenes with Fully Saturated and Thermally Stable Cl Terminations. *Nanoscale Adv.* **2019**, *1*, 3680–3685.

7. Kobayashi, T.; Sun, Y.; Prenger, K.; Jiang, D.-e.; Naguib, M.; Pruski, M. Nature of Terminating Hydroxyl Groups and Intercalating Water in $Ti_3C_2T_x$ MXenes: A Study by ^{1}H Solid-State NMR and DFT Calculations. *J. Phys. Chem. C* **2020**, *124*, 13649–13655.

8. Naguib, M.; Mashtalir, O.; Carle, J.; Presser, V.; Lu, J.; Hultman, L.; Gogotsi, Y.; Barsoum, M. W. Two-dimensional Transition Metal Carbides. *ACS Nano* **2012**, *6*, 1322–1331.

9. Barsoum, M. W. *MAX phases: properties of machinable ternary carbides and nitrides*; John Wiley & Sons, 2013.

10. Anasori, B.; Lukatskaya, M. R.; Gogotsi, Y. 2D Metal Carbides and Nitrides (MXenes) for Energy Storage. *Nat. Rev. Mater.* **2017**, *2*, 1–17.

11. Tang, Q.; Zhou, Z.; Shen, P. Are MXenes Promising Anode Materials for Li Ion Batteries? Computational Studies on Electronic Properties and Li Storage Capability of Ti_3C_2 and $Ti_3C_2X_2$ (X= F, OH) Monolayer. *J. Am. Chem. Soc.* **2012**, *134*, 16909–16916.

12. Lukatskaya, M. R.; Mashtalir, O.; Ren, C. E.; Dall'Agnese, Y.; Rozier, P.; Taberna, P. L.; Naguib, M.; Simon, P.; Barsoum, M. W.; Gogotsi, Y. Cation Intercalation and High Volumetric Capacitance of Two-dimensional Titanium Carbide. *Science* **2013**, *341*, 1502–1505.

13. Er, D.; Li, J.; Naguib, M.; Gogotsi, Y.; Shenoy, V. B. Ti_3C_2 MXene as a High Capacity Electrode Material for Metal (Li, Na, K, Ca) Ion Batteries. *ACS Appl. Mater. Interfaces* **2014**, *6*, 11173–11179.

14. Liang, X.; Garsuch, A.; Nazar, L. F. Sulfur Cathodes based on Conductive MXene Nanosheets for High-performance Lithium–sulfur Batteries. *Angew. Chem.* **2015**, *127*, 3979–3983.

15. Wang, X.; Kajiyama, S.; Iinuma, H.; Hosono, E.; Oro, S.; Moriguchi, I.; Okubo, M.; Yamada, A. Pseudocapacitance of MXene Nanosheets for High-power Sodium-ion Hybrid Capacitors. *Nat. Commun.* **2015**, *6*, 1–6.

16. Xia, Y.; Mathis, T. S.; Zhao, M.-Q.; Anasori, B.; Dang, A.; Zhou, Z.; Cho, H.; Gogotsi, Y.; Yang, S. Thickness-independent Capacitance of Vertically Aligned Liquid-crystalline MXenes. *Nature* **2018**, *557*, 409–412.

17. Shahzad, F.; Alhabeb, M.; Hatter, C. B.; Anasori, B.; Hong, S. M.; Koo, C. M.; Gogotsi, Y. Electromagnetic Interference Shielding with 2D Transition Metal Carbides (MXenes). *Science* **2016**, *353*, 1137–1140.

18. Seh, Z. W.; Fredrickson, K. D.; Anasori, B.; Kibsgaard, J.; Strickler, A. L.; Lukatskaya, M. R.; Gogotsi, Y.; Jaramillo, T. F.; Vojvodic, A. Two-dimensional Molyb-

denum Carbide (MXene) as an Efficient Electrocatalyst for Hydrogen Evolution. *ACS Energy Lett.* **2016**, *1*, 589–594.

19. Lind, H.; Wickman, B.; Halim, J.; Montserrat-Sisó, G.; Hellman, A.; Rosen, J. Hydrogen Evolution Reaction for Vacancy-Ordered i-MXenes and the Impact of Proton Absorption into the Vacancies. *Adv. Sustainable Syst.* **2021**, *5*, 2000158.

20. Li, R.; Zhang, L.; Shi, L.; Wang, P. MXene Ti_3C_2: an Effective 2D Light-to-heat Conversion Material. *ACS Nano* **2017**, *11*, 3752–3759.

21. Li, N.; Chen, X.; Ong, W.-J.; MacFarlane, D. R.; Zhao, X.; Cheetham, A. K.; Sun, C. Understanding of Electrochemical Mechanisms for CO_2 Capture and Conversion into Hydrocarbon Fuels in Transition-metal Carbides (MXenes). *ACS Nano* **2017**, *11*, 10825–10833.

22. Ren, C. E.; Hatzell, K. B.; Alhabeb, M.; Ling, Z.; Mahmoud, K. A.; Gogotsi, Y. Charge- and size-selective Ion Sieving through $Ti_3C_2T_x$ MXene Membranes. *J. Phys. Chem. Lett.* **2015**, *6*, 4026–4031.

23. Verger, L.; Natu, V.; Carey, M.; Barsoum, M. W. MXenes: an Introduction of their Synthesis, Select Properties, and Applications. *Trends Chem.* **2019**, *1*, 656–669.

24. Ekimov, A. I.; Onushchenko, A. A. Quantum Size Effect in Three-dimensional Microscopic Semiconductor Crystals. *JETP Lett.* **1981**, *34*, 345–349.

25. Ashoori, R. Electrons in Artificial Atoms. *Nature* **1996**, *379*, 413–419.

26. Alivisatos, A. P. Semiconductor Clusters, Nanocrystals, and Quantum Dots. *Science* **1996**, *271*, 933–937.

27. Xu, Q.; Ding, L.; Wen, Y.; Yang, W.; Zhou, H.; Chen, X.; Street, J.; Zhou, A.; Ong, W.-J.; Li, N. High Photoluminescence Quantum Yield of 18.7% by Using Nitrogen-doped Ti_3C_2 MXene Quantum Dots. *J. Mater. Chem. C* **2018**, *6*, 6360–6369.

28. Xu, G.; Niu, Y.; Yang, X.; Jin, Z.; Wang, Y.; Xu, Y.; Niu, H. Preparation of $Ti_3C_2T_x$ MXene-derived Quantum Dots with White/Blue-emitting Photoluminescence and Electrochemiluminescence. *Adv. Opt. Mater.* **2018**, *6*, 1800951.

29. Lu, S.; Sui, L.; Liu, Y.; Yong, X.; Xiao, G.; Yuan, K.; Liu, Z.; Liu, B.; Zou, B.; Yang, B. White Photoluminescent Ti_3C_2 MXene Quantum Dots with Two-photon Fluorescence. *Adv. Sci.* **2019**, *6*, 1801470.

30. Xu, Q.; Yang, W.; Wen, Y.; Liu, S.; Liu, Z.; Ong, W.-J.; Li, N. Hydrochromic Full-color MXene Quantum Dots through Hydrogen Bonding toward Ultrahigh-efficiency White Light-emitting Diodes. *Appl. Mater. Today* **2019**, *16*, 90–101.

31. Guan, Q.; Ma, J.; Yang, W.; Zhang, R.; Zhang, X.; Dong, X.; Fan, Y.; Cai, L.; Cao, Y.; Zhang, Y., *et al.* Highly Fluorescent Ti_3C_2 MXene Quantum Dots for Macrophage Labeling and Cu^{2+} Ion Sensing. *Nanoscale* **2019**, *11*, 14123–14133.

32. Zhang, Q.; Sun, Y.; Liu, M.; Liu, Y. Selective Detection of F^{3+} Ions based on Fluorescence MXene Quantum Dots via a Mechanism Integrating Electron Transfer and Inner Filter Effect. *Nanoscale* **2020**, 1826.

33. Feng, Y.; Zhou, F.; Deng, Q.; Peng, C. Solvothermal Synthesis of in situ Nitrogen-doped Ti_3C_2 MXene Fluorescent Quantum Dots for Selective Cu^{2+} Detection. *Ceram. Int.* **2020**, *46*, 8320–8327.

34. Yu, X.; Cai, X.; Cui, H.; Lee, S.-W.; Yu, X.-F.; Liu, B. Fluorine-free Preparation of Titanium Carbide MXene Quantum Dots with High Near-infrared Photothermal Performances for Cancer Therapy. *Nanoscale* **2017**, *9*, 17859–17864.

35. Xue, Q.; Zhang, H.; Zhu, M.; Pei, Z.; Li, H.; Wang, Z.; Huang, Y.; Huang, Y.; Deng, Q.; Zhou, J., *et al.* Photoluminescent Ti_3C_2 MXene Quantum Dots for Multicolor Cellular Imaging. *Adv. Mater.* **2017**, *29*, 1604847.

36. Cai, G.; Yu, Z.; Tong, P.; Tang, D. Ti$_3$C$_2$ MXene Quantum Dot-encapsulated Liposomes for Photothermal Immunoassays using a Portable Near-infrared Imaging Camera on a Smartphone. *Nanoscale* **2019**, *11*, 15659–15667.

37. Chen, X.; Sun, X.; Xu, W.; Pan, G.; Zhou, D.; Zhu, J.; Wang, H.; Bai, X.; Dong, B.; Song, H. Ratiometric Photoluminescence Sensing Bbased on Ti$_3$C$_2$ MXene Quantum Dots as an Intracellular pH Sensor. *Nanoscale* **2018**, *10*, 1111–1118.

38. Guo, Z.; Zhu, X.; Wang, S.; Lei, C.; Huang, Y.; Nie, Z.; Yao, S. Fluorescent Ti$_3$C$_2$ MXene Quantum Dots for an Alkaline Phosphatase Assay and Embryonic Stem Cell Identification Based on the Inner Filter Effect. *Nanoscale* **2018**, *10*, 19579–19585.

39. Lu, Q.; Wang, J.; Li, B.; Weng, C.; Li, X.; Yang, W.; Yan, X.; Hong, J.; Zhu, W.; Zhou, X. Dual-Emission Reverse Change Ratio Photoluminescence Sensor Based on a Probe of Nitrogen-Doped Ti$_3$C$_2$ Quantum Dots@DAP to Detect H$_2$O$_2$ and Xanthine. *Anal. Chem.* **2020**, *92*, 7770–7777.

40. Zeng, Z.; Yan, Y.; Chen, J.; Zan, P.; Tian, Q.; Chen, P. Boosting the Photocatalytic Ability of Cu$_2$O Nanowires for CO$_2$ Conversion by MXene Quantum Dots. *Adv. Funct. Mater.* **2019**, *29*, 1806500.

41. Yang, X.; Jia, Q.; Duan, F.; Hu, B.; Wang, M.; He, L.; Song, Y.; Zhang, Z. Multiwall Carbon Nanotubes Loaded with MoS$_2$ Quantum Dots and MXene Quantum Dots: Non–Pt Bifunctional Catalyst for the Methanol Oxidation and Oxygen Reduction Reactions in Alkaline Solution. *Appl. Surf. Sci.* **2019**, *464*, 78–87.

42. Tang, R.; Zhou, S.; Li, C.; Chen, R.; Zhang, L.; Zhang, Z.; Yin, L. Janus-Structured Co-Ti$_3$C$_2$ MXene Quantum Dots as a Schottky Catalyst for High-Performance Photo-electrochemical Water Oxidation. *Adv. Funct. Mater.* **2020**, 2000637.

43. Wang, H.; Zhao, R.; Hu, H.; Fan, X.; Zhang, D.; Wang, D. 0D/2D Heterojunctions of Ti$_3$C$_2$ MXene QDs/SiC as an Efficient and Robust Photocatalyst for Boosting the Visible

Photocatalytic NO Pollutant Removal Ability. *ACS Appl. Mater. Interfaces* **2020**, *12*, 40176–40185.

44. Du, X.; Zhao, T.; Xiu, Z.; Xing, Z.; Li, Z.; Pan, K.; Yang, S.; Zhou, W. BiVO$_4$@ ZnIn$_2$S$_4$/Ti$_3$C$_2$ MXene Quantum Dots Assembly All-solid-state Direct Z-scheme Photo-catalysts for Efficient Visible-light-driven Overall Water Splitting. *Appl. Mater. Today* **2020**, 100719.

45. Chen, X.; Xu, W.; Ding, N.; Ji, Y.; Pan, G.; Zhu, J.; Zhou, D.; Wu, Y.; Chen, C.; Song, H. Dual Interfacial Modification Engineering with 2D MXene Quantum Dots and Copper Sulphide Nanocrystals Enabled High-Performance Perovskite Solar Cells. *Adv. Funct. Mater.* **2020**, 2003295.

46. Qin, Y.; Wang, Z.; Liu, N.; Sun, Y.; Han, D.; Liu, Y.; Niu, L.; Kang, Z. High-yield Fabri-cation of Ti$_3$C$_2$T$_x$ MXene Quantum Dots and Their Electrochemiluminescence Behavior. *Nanoscale* **2018**, *10*, 14000–14004.

47. Rafieerad, A.; Yan, W.; Sequiera, G. L.; Sareen, N.; Abu-El-Rub, E.; Moudgil, M.; Dhingra, S. Application of Ti$_3$C$_2$ MXene Quantum Dots for Immunomodulation and Regenerative Medicine. *Adv. Healthcare Mater.* **2019**, *8*, 1900569.

48. Chen, X.; Li, J.; Pan, G.; Xu, W.; Zhu, J.; Zhou, D.; Li, D.; Chen, C.; Lu, G.; Song, H. Ti$_3$C$_2$ MXene Quantum Dots/TiO$_2$ Inverse Opal Heterojunction Electrode Platform for Superior Photoelectrochemical Biosensing. *Sens. Actuators, B* **2019**,

49. Liu, M.; Zhou, J.; He, Y.; Cai, Z.; Ge, Y.; Zhou, J.; Song, G. ε-Poly-L-lysine-protected Ti$_3$C$_2$ MXene Quantum Dots with High Quantum Yield for Fluorometric Determination of Cytochrome c and Trypsin. *Microchim. Acta* **2019**, *186*, 770.

50. He, F.; Zhu, B.; Cheng, B.; Yu, J.; Ho, W.; Macyk, W. 2D/2D/0D TiO$_2$/C$_3$N$_4$/Ti$_3$C$_2$ MXene Composite S-scheme Photocatalyst with Enhanced CO$_2$ Reduction Activity. *Appl. Catal., B* **2020**, 119006.

51. Liu, M.; He, Y.; Zhou, J.; Ge, Y.; Zhou, J.; Song, G. A "Naked-eye" Aolorimetric and Ratiometric Fluorescence Probe for Uric Acid Based on Ti_3C_2 MXene Quantum Dots. *Anal. Chim. Acta* **2020**, *1103*, 134–142.

52. Gu, M.; Dai, Z.; Yan, X.; Ma, J.; Niu, Y.; Lan, W.; Wang, X.; Xu, Q. Comparison of Toxicity of Ti_3C_2 and Nb_2C Mxene Quantum Dots (QDs) to Human Umbilical Vein Endothelial Cells. *J. Appl. Toxicol.* **2020**, 1–10.

53. Liu, M.; Bai, Y.; He, Y.; Zhou, J.; Ge, Y.; Zhou, J.; Song, G. Facile Microwave-assisted Synthesis of Ti_3C_2 MXene Quantum Dots for Ratiometric Fluorescence Detection of Hypochlorite. *Microchim. Acta* **2021**, *188*, 1–8.

54. Zhao, L.; Wang, Z.; Li, Y.; Wang, S.; Wang, L.; Qi, Z.; Ge, Q.; Liu, X.; Zhang, J. Z. Designed Synthesis of Chlorine and Nitrogen co-doped Ti_3C_2 MXene Quantum Dots and their Outstanding Hydroxyl Radical Scavenging Properties. *J. Mater. Sci. Technol.* **2021**, *78*, 30–37.

55. Rezk, A. R.; Tan, J. K.; Yeo, L. Y. HYbriD Resonant Acoustics (HYDRA). *Adv. Mater.* **2016**, *28*, 1970–1975.

56. Rezk, A. R.; Ahmed, H.; Brain, T. L.; Castro, J. O.; Tan, M. K.; Langley, J.; Cox, N.; Mondal, J.; Li, W.; Ashokkumar, M., *et al.* Free Radical Generation From High-frequency Electromechanical Dissociation of Pure Water. *J. Phys. Chem. Lett.* **2020**, *11*, 4655–4661.

57. Rezk, A. R.; Ahmed, H.; Ramesan, S.; Yeo, L. Y. High Frequency Sonoprocessing: A New Field of Cavitation-Free Acoustic Materials Synthesis, Processing, and Manipulation. *Adv. Sci.* **2021**, *8*, 2001983.

58. Ahmed, H.; Rezk, A. R.; Carey, B. J.; Wang, Y.; Mohiuddin, M.; Berean, K. J.; Russo, S. P.; Kalantar-zadeh, K.; Yeo, L. Y. Ultrafast Acoustofluidic Exfoliation of Stratified Crystals. *Adv. Mater.* **2018**, *30*, 1704756.

59. Mohiuddin, M.; Wang, Y.; Zavabeti, A.; Syed, N.; Datta, R. S.; Ahmed, H.; Daeneke, T.; Russo, S. P.; Rezk, A. R.; Yeo, L. Y., *et al.* Liquid Phase Acoustic WaveExfoliation of Layered MoS_2: Critical Impact of Electric Field in Efficiency. *Chem. Mater.* **2018**, *30*, 5593–5601.

60. Marqus, S.; Ahmed, H.; Ahmed, M.; Xu, C.; Rezk, A. R.; Yeo, L. Y. Increasing Exfoliation Yield in the Synthesis of MoS_2 Quantum Dots for Optoelectronic and Other Applications Through a Continuous Multicycle Acoustomicrofluidic Approach. *ACS Appl. Nano Mater.* **2018**, *1*, 2503–2508.

61. Ahmed, M.; Ahmed, H.; Rezk, A. R.; Yeo, L. Y. Rapid Dry Exfoliation Method for Tuneable Production of Molybdenum Disulphide Quantum Dots and Large Micron-dimension Sheets. *Nanoscale* **2019**, *11*, 11626–11633.

62. Ghazaly, A. E.; Ahmed, H.; Rezk, A. R.; Halim, J.; Persson, P. O.; Yeo, L. Y.; Rosen, J. Ultrafast, One-Step, Salt-Solution-Based Acoustic Synthesis of Ti3C2 MXene. *ACS nano* **2021**,

63. Mashtalir, O.; Naguib, M.; Mochalin, V. N.; Dall'Agnese, Y.; Heon, M.; Barsoum, M. W.; Gogotsi, Y. Intercalation and Delamination of Layered Carbides and Carbonitrides. *Nat. Commun.* **2013**, *4*, 1–7.

64. Naguib, M.; Unocic, R. R.; Armstrong, B. L.; Nanda, J. Large-scale Delamination of Multi-layers Transition Metal Carbides and Carbonitrides "MXenes". *Dalt. Trans.* **2015**, *44*, 9353–9358.

65. Ghidiu, M.; Lukatskaya, M. R.; Zhao, M.-Q.; Gogotsi, Y.; Barsoum, M. W. Conductive Two-dimensional Titanium Carbide 'Clay' with High Volumetric Capacitance. *Nature* **2014**, *516*, 78–81.

66. Kalambate, P. K.; Gadhari, N. S.; Li, X.; Rao, Z.; Navale, S. T.; Shen, Y.; Patil, V. R.;

Huang, Y. Recent Advances in MXene–based Electrochemical Sensors and Biosensors. *Trends Anal. Chem.* **2019**, *120*, 115643.

67. Li, X.; Liu, F.; Huang, D.; Xue, N.; Dang, Y.; Zhang, M.; Zhang, L.; Li, B.; Liu, D.; Wang, L., *et al.* Nonoxidized Mxene Quantum Dots Prepared by Microexplosion Method for Cancer Catalytic Therapy. *Adv. Funct. Mater.* **2020**, *30*, 2000308.

68. Lipatov, A.; Lu, H.; Alhabeb, M.; Anasori, B.; Gruverman, A.; Gogotsi, Y.; Sinitskii, A. Elastic Properties of 2D $Ti_3C_2T_x$ MXene Monolayers and Bilayers. *Sci. Adv.* **2018**, *4*, eaat0491.

69. Alhabeb, M.; Maleski, K.; Anasori, B.; Lelyukh, P.; Clark, L.; Sin, S.; Gogotsi, Y. Guidelines for Synthesis and Processing of Two-dimensional Titanium Carbide ($Ti_3C_2T_x$ MXene). *Chem. Mater.* **2017**, *29*, 7633–7644.

70. Shuck, C. E.; Sarycheva, A.; Anayee, M.; Levitt, A.; Zhu, Y.; Uzun, S.; Balitskiy, V.; Zahorodna, V.; Gogotsi, O.; Gogotsi, Y. Scalable Synthesis of $Ti_3C_2T_x$ MXene. *Adv. Eng. Mater.* **2020**, *22*, 1901241.

71. Li, G.; Tan, L.; Zhang, Y.; Wu, B.; Li, L. Highly Efficiently Delaminated Single-layered MXene Nanosheets with Large Lateral Size. *Langmuir* **2017**, *33*, 9000–9006.

72. Ghidiu, M.; Barsoum, M. W. The 110 Reflection in X-ray Diffraction of MXene Films: Misinterpretation and Measurement via Non-standard Orientation. *J. Am. Ceram. Soc.* **2017**, *100*, 5395–5399.

73. Halim, J.; Cook, K. M.; Naguib, M.; Eklund, P.; Gogotsi, Y.; Rosen, J.; Barsoum, M. W. X-ray Photoelectron Spectroscopy of Select Multi-layered Transition Metal Carbides (MXenes). *Appl. Surf. Sci.* **2016**, *362*, 406–417.

74. Halim, J.; Persson, I.; Eklund, P.; Persson, P. O.; Rosen, J. Sodium Hydroxide and Vac-

uum Annealing Modifications of the Surface Terminations of a Ti_3C_2 (MXene) Epitaxial Thin Film. *RSC Adv.* **2018**, *8*, 36785–36790.

75. Thamaphat, K.; Limsuwan, P.; Ngotawornchai, B. Phase characterization of TiO2 powder by XRD and TEM. *Agric. Nat. Resour.* **2008**, *42*, 357–361.

76. Lorencova, L.; Bertok, T.; Dosekova, E.; Holazova, A.; Paprckova, D.; Vikartovska, A.; Sasinkova, V.; Filip, J.; Kasak, P.; Jerigova, M., *et al.* Electrochemical Performance of $Ti_3C_2T_x$ MXene in Aqueous Media: towards Ultrasensitive H_2O_2 Sensing. *Electrochim. Acta* **2017**, *235*, 471–479.

77. Maleski, K.; Mochalin, V. N.; Gogotsi, Y. Dispersions of Two-dimensional Titanium Carbide MXene in Organic Solvents. *Chem. Mater.* **2017**, *29*, 1632–1640.

78. Qi, A.; Yeo, L. Y.; Friend, J. R. Interfacial Destabilization and Atomization Driven by Surface Acoustic Waves. *Phys. Fluids* **2008**, *20*, 074103.

TOC Graphic